

TRAJECTORY DESIGN LEVERAGING LOW-THRUST, MULTI-BODY EQUILIBRIA AND THEIR MANIFOLDS

Andrew D. Cox*, Kathleen C. Howell† and David C. Folta‡

A key challenge in low-thrust trajectory design is generating preliminary solutions that simultaneously specify the spacecraft position and velocity vectors, as well as the thrust history. To mitigate this difficulty, dynamical structures within a combined low-thrust circular restricted 3-body problem (CR3BP) are investigated as candidate solutions to seed initial low-thrust trajectory designs. The addition of low-thrust to the CR3BP modifies the locations and stability of the equilibria, offering novel geometries for mission applications. Transfers between these novel equilibria are constructed by leveraging the associated stable and unstable manifolds and insights from the low-thrust CR3BP.

INTRODUCTION

A key challenge in low-thrust trajectory design is generating preliminary solutions that simultaneously deliver spacecraft position and velocity vectors through time, as well as the thrust history. Although many strategies have emerged to construct spacecraft position and velocity histories in dynamical models such as the circular restricted 3-body problem (CR3BP), fewer methodologies are available to identify a preliminary thrust history. Those methods that do exist often rely on optimization algorithms to solve boundary value or initial value problems that include the control variables. For example, predictor-corrector shooting algorithms have been applied to generate control histories along low-thrust transfers between periodic orbits in the CR3BP.^{1,2} Other authors have applied low-thrust to natural arcs via optimization processes or machine learning to identify *attainable regions*.^{3,4} Similarly, collocation and direct transcription, combined with indirect optimization, are leveraged to construct non-intuitive orbit geometries by leveraging a low-thrust acceleration.^{5,6}

Rather than rely solely on numerical methods and optimization algorithms to develop a low-thrust control history, dynamical systems techniques are applied to a combined low-thrust, CR3BP (CR3BP-LT) model to gain insights to be applied for the construction of preliminary solutions that include low-thrust arcs. Guidance from the CR3BP is already available for ballistic trajectories; dynamical structures such as equilibrium solutions, forbidden regions, periodic orbits, and invariant manifolds describe flow throughout the system.⁷ These structures are leveraged in numerous mission scenarios and are valuable guides for trajectory design.^{8,9,10,11} Similar structures and insights are available from the CR3BP-LT to supply a larger array of design options than are currently available for low-thrust trajectory design.¹² Subsequently, optimal low-thrust paths that depend strongly

*Ph.D. Student, School of Aeronautics and Astronautics, Purdue University, West Lafayette, IN 47907; cox50@purdue.edu

†Hsu Lo Distinguished Professor of Aeronautics and Astronautics, School of Aeronautics and Astronautics, Purdue University, West Lafayette, IN 47907; howell@purdue.edu

‡Senior Fellow, NASA Goddard Space Flight Center, Greenbelt, MD, 20771; david.c.folta@nasa.gov

on the initial design input to an optimization or other numerical algorithm may be tailored more specifically to a particular mission scenario.

Two key properties of the CR3BP-LT are leveraged to inform low-thrust trajectory design in this analysis. First, by employing a set of simplifying assumptions, the CR3BP-LT is reduced to a conservative, Hamiltonian system. The natural energy (i.e., the Jacobi constant) varies when low-thrust is included, but evolves independently of the spacecraft path and is described by a plane in x - y -energy space. This geometric result supplies intuition to facilitate the otherwise difficult selection of thrust parameters for an initial design. Second, the equilibrium solutions in the planar CR3BP-LT occur in unique configurations with manifolds that guide global flow in novel ways. The number and locations of the low-thrust equilibria vary with the magnitude and orientation of the low-thrust acceleration vector, including equilibrium point configurations not available in the natural model.^{12,13,14} Additionally, the stability properties of the low-thrust equilibria vary with position and differ from the natural CR3BP equilibria, supplying stable and unstable manifolds that describe new flow patterns through the system. By leveraging these manifolds, low-thrust transfers between the natural Lagrange points (and the nearby oscillatory motion) are constructed.¹³ This strategy, introduced by Farrés for Sun-Earth solar sail applications, is extended to the Earth-Moon system and additional insights from the CR3BP-LT are employed to guide the design.

DYNAMICAL MODEL DEVELOPMENT

The first step in computing and leveraging dynamical structures within the CR3BP-LT is the development of the dynamical model. An energy-based approach is first employed to derive the governing equations in the CR3BP and obtain an expression for the natural Hamiltonian. By augmenting the CR3BP equations of motion (EOMs) with a low-thrust term, the CR3BP-LT is constructed and the associated low-thrust Hamiltonian is defined. This low-thrust Hamiltonian serves as an integral of the motion when the low-thrust acceleration vector is fixed in the rotating frame, and, thus, may be leveraged to characterize motion in the CR3BP-LT.

Circular Restricted 3-Body Problem

The CR3BP describes the motion of a relatively small body, such as a spacecraft, in the presence of two larger gravitational point masses (P_1 and P_2) with paths that evolve along circular orbits about their mutual barycenter (B). To simplify the governing equations and enable straightforward visualization of periodic solutions, the motion of the spacecraft is described in a right-handed frame (\hat{x} , \hat{y} , \hat{z}) that rotates with the two primaries, as seen in Figure 1, where \hat{x} , \hat{y} , and \hat{z} are vectors of unit length. The system is parameterized by the mass ratio, $\mu = M_2/(M_1 + M_2)$, where M_1 and M_2 are the masses of the primaries and $M_1 \geq M_2$. To facilitate numerical integration, the dimensional values are nondimensionalized by characteristic quantities such that the distance between P_1 and P_2 is unity, the mean motion of the two primaries is unity, and the masses of each body range from zero to one half.¹⁵ The spacecraft is located relative to the system barycenter in the rotating frame via the vector $\vec{r} = \{x \ y \ z\}^T$.

The equations of motion governing the CR3BP are derived via a Hamiltonian energy approach.

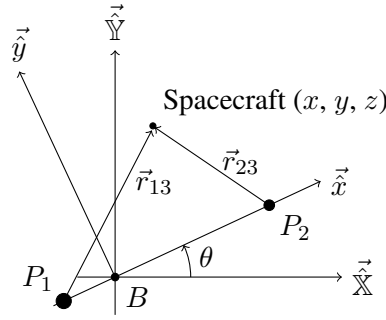


Figure 1. CR3BP system configuration; two point masses, P_1 and P_2 , proceed on circular orbits about their mutual barycenter, B . The behavior of a third, relatively massless particle is described within the rotating coordinate frame, $(\hat{x}, \hat{y}, \hat{z})$

Let the kinetic (T) and potential (V) energies corresponding to the CR3BP system be defined by

$$T = \frac{1}{2} \left[(\dot{x} - y)^2 + (\dot{y} + x)^2 + \dot{z}^2 \right], \quad (1)$$

$$V = \frac{-(1-\mu)}{r_{13}} - \frac{\mu}{r_{23}}, \quad (2)$$

where \dot{x} , \dot{y} , and \dot{z} are the derivatives of the position states with respect to nondimensional time as observed in the rotating frame, and r_{13} and r_{23} are the distances between the spacecraft (P_3) and the first and second primaries, respectively:

$$r_{13} = \sqrt{(x + \mu)^2 + y^2 + z^2}, \quad r_{23} = \sqrt{(x - 1 + \mu)^2 + y^2 + z^2}.$$

Next, form the Hamiltonian,

$$H_{nat} = \frac{1}{2}v^2 - \frac{1}{2}(x^2 + y^2) - \frac{1-\mu}{r_{13}} - \frac{\mu}{r_{23}}, \quad (3)$$

where the squared velocity magnitude is $v^2 = \dot{x}^2 + \dot{y}^2 + \dot{z}^2$. By applying Hamilton's canonical equations of motion, a set of differential equations that govern the motion of P_3 emerges,

$$\ddot{x} = 2\dot{y} + \Omega_x, \quad (4)$$

$$\ddot{y} = -2\dot{x} + \Omega_y, \quad (5)$$

$$\ddot{z} = \Omega_z, \quad (6)$$

where Ω is the CR3BP *pseudo-potential* function,

$$\Omega = \frac{1}{2}(x^2 + y^2) + \frac{1-\mu}{r_{13}} + \frac{\mu}{r_{23}}, \quad (7)$$

and Ω_x , Ω_y , and Ω_z represent the partial derivative of Ω with respect to the subscripted variables x , y , and z , respectively. Because the CR3BP is autonomous and conservative, H_{nat} is constant and equivalent to the Jacobi integral, i.e., the *Jacobi constant*. The Jacobi constant, $C = -2H_{nat}$, is commonly leveraged as a measure of the energy associated with arcs in the CR3BP.

CR3BP Incorporating Low-Thrust

To incorporate low-thrust into the CR3BP multi-body model, the low-thrust acceleration vector is first defined. This vector,

$$\vec{a}_{lt} = \frac{f}{m} \hat{u}, \quad (8)$$

is oriented relative to the rotating frame via the unit vector \hat{u} and scaled by the nondimensional thrust magnitude, f , and nondimensional spacecraft mass, $m = M_3/M_{3,0}$, where M_3 is the instantaneous spacecraft mass and $M_{3,0}$ is the initial (wet) spacecraft mass. The nondimensionalization of the thrust magnitude leverages the CR3BP characteristic time, t_* , and characteristic length, l_* , for consistency with the CR3BP coordinate nondimensionalization, i.e.,

$$f = \frac{F t_*^2}{l_* M_{3,0}}. \quad (9)$$

In this expression, F describes the thrust magnitude in kilonewtons, l_* represents the distance between P_1 and P_2 in kilometers, t_* is the inverted system mean motion, $t_* = 1/n$, in seconds, and $M_{3,0}$ is defined in terms of kilograms. A nondimensional thrust magnitude of $f \approx 10^{-2}$ in the Earth-Moon and Sun-Earth CR3BP-LT systems is consistent with current spacecraft capabilities, such as Deep Space 1, Dawn, or Hayabusa.¹² Accordingly, a low-thrust acceleration magnitude of $a_{lt} = f/m = 7e-2$ is frequently leveraged in this document to represent a reasonable low-thrust capability in the Earth-Moon system.

To apply an energy-based derivation of the CR3BP-LT EOMs similar to the derivation leveraged for the CR3BP, the CR3BP dynamics are augmented with a low-thrust acceleration term. While the spacecraft kinetic energy expression in Equation (1) remains unchanged, the potential energy expression incorporates a low-thrust acceleration term, i.e.,

$$V_{lt} = \frac{-(1-\mu)}{r_{13}} - \frac{\mu}{r_{23}} - \vec{r} \cdot \vec{a}_{lt}. \quad (10)$$

This additional term propagates through the derivation to yield the low-thrust Hamiltonian,

$$H_{lt} = \frac{1}{2}v^2 - \frac{1}{2}(x^2 + y^2) - \frac{1-\mu}{r_{13}} - \frac{\mu}{r_{23}} - \vec{r} \cdot \vec{a}_{lt}, \quad (11)$$

which may also be written in terms of the natural Hamiltonian, i.e.,

$$H_{lt} = H_{nat} - \vec{r} \cdot \vec{a}_{lt}. \quad (12)$$

Due to the time-varying nature of the spacecraft mass, the governing equations are not available directly from Hamilton's canonical equations. However, Newton's law is straightforwardly applied to yield the EOMs,

$$\ddot{x} = 2\dot{y} + \Omega_x + a_{lt}u_x, \quad (13)$$

$$\ddot{y} = -2\dot{x} + \Omega_y + a_{lt}u_y, \quad (14)$$

$$\ddot{z} = \Omega_z + a_{lt}u_z, \quad (15)$$

$$\dot{m} = \frac{-f l_*}{I_{sp} g_0 t_*}, \quad (16)$$

where a_{lt} is the magnitude of the low-thrust acceleration vector, u_x , u_y , and u_z are the individual components of \hat{u} along each of the rotating axes, I_{sp} is the specific impulse associated with the propulsion system, and $g_0 = 9.80665e-3$ km/s². These equations are consistent with those that govern the natural CR3BP and are simply augmented with the low-thrust acceleration terms.

CR3BP-LT Simplifications for Global Insight

To facilitate analyses in the CR3BP-LT, simplifications are applied to reduce the number of dimensions. The conservative, natural problem admits an integral of the motion (the Hamiltonian, H_{nat}), reducing the natural problem dimension by one. However, due to the non-autonomous nature of the CR3BP-LT, the low-thrust Hamiltonian is not constant in general and, thus, does not necessarily offer a similar dimension reduction in the low-thrust problem. Nevertheless, an analysis of the time derivative of the low-thrust Hamiltonian supplies useful insights. First, differentiate the first term in Equation (12), i.e., the expression for the natural Hamiltonian,

$$\frac{\partial H_{nat}}{\partial \tau} = \dot{x}(\ddot{x} - \Omega_x) + \dot{y}(\ddot{y} - \Omega_y) + \dot{z}(\ddot{z} - \Omega_z). \quad (17)$$

Substitute the CR3BP-LT equations of motion from Equations (13) – (16) into this derivative expression and simplify:

$$\frac{\partial H_{nat}}{\partial \tau} = \dot{x}(2\dot{y} + a_{lt}u_x) + \dot{y}(-2\dot{x} + a_{lt}u_y) + \dot{z}a_{lt}u_z = \vec{v} \cdot \vec{a}_{lt}, \quad (18)$$

where $\vec{v} = \{\dot{x} \ \dot{y} \ \dot{z}\}^T$ is the spacecraft velocity vector in the rotating frame. The derivative of the second term in Equation (12) is straightforwardly evaluated,

$$\frac{\partial}{\partial \tau} [\vec{r} \cdot \vec{a}_{lt}] = \vec{v} \cdot \vec{a}_{lt} + \vec{r} \cdot \dot{\vec{a}}_{lt}. \quad (19)$$

Combine Equations (18) and (19) to yield the time derivative of H_{lt} ,

$$\frac{\partial H_{lt}}{\partial \tau} = -\vec{r} \cdot \dot{\vec{a}}_{lt}. \quad (20)$$

If \vec{a}_{lt} is constant, both in magnitude and orientation as viewed in the rotating frame, $\dot{\vec{a}}_{lt} = \vec{0}$ and H_{lt} is constant during low-thrust propagations. That is, if \vec{a}_{lt} is constant, the CR3BP-LT is a conservative system and the low-thrust Hamiltonian may be leveraged as an integral of the motion in the low-thrust problem.

While preserving a fixed orientation, i.e., a fixed \hat{u} vector, is a familiar attitude control strategy, preserving a constant acceleration magnitude, a_{lt} , is less common. Consider the expression, $a_{lt} = f/m$ with a fixed orientation and a fixed thrust magnitude ($\hat{u} = \text{constant}$, $f = \text{constant}$) but with variable mass. Accordingly, the time derivative of \vec{a}_{lt} , evaluated as

$$\dot{\vec{a}}_{lt} = \frac{f\dot{m}}{m^2}\hat{u} = -a_{lt}^2 \frac{l_*}{I_{sp}g_0 t_*} \hat{u}, \quad (21)$$

is non-zero when $\dot{m} \neq 0$. To determine if the derivative magnitude, $\dot{a}_{lt} = -a_{lt}^2 l_*/(I_{sp}g_0 t_*)$, is sufficiently small to be ignored, compare \dot{a}_{lt} with the energy range across the natural equilibrium solutions, i.e., the H_{nat} values associated with the CR3BP Lagrange points. In the Earth-Moon CR3BP-LT, this energy range, $H_{nat}(L_5) - H_{nat}(L_1)$, where L_5 and L_1 are the natural equilibria with the highest and lowest energies, respectively, is several orders of magnitude larger than \dot{a}_{lt} . Subsequently, the variations in H_{lt} due to the time-varying spacecraft mass are very small compared to the $L_5 \rightarrow L_1$ energy range, and H_{lt} is reasonably approximated as a constant for propagations with a maximum mass consumption of 15%, i.e., propagations with $m(\tau) > 0.85$. However, this assumption is not applicable to all three-body systems, particularly those with large

l_*/t_* ratios (resulting in a large $\dot{\vec{a}}_{lt}$ magnitude) and those with very small $L_5 \rightarrow L_1$ energy ranges, e.g., the Sun-Earth system. In such systems, the characteristic quantities may be adjusted to produce an l_*/t_* ratio that sufficiently decreases the magnitude of the H_{lt} derivative. As the analyses in this investigation leverage the dynamics of the Earth-Moon system, a_{lt} and H_{lt} are assumed constant without adjustment of the characteristic quantities such that the resulting dynamical properties may be leveraged to inform the low-thrust trajectory design problem. Accordingly, the variable acceleration quantity f/m is replaced by the constant value a_{lt} , removing the need for the mass time-derivative in Equation (16). These simplifications – a constant low-thrust Hamiltonian and a constant acceleration magnitude – effectively reduce the problem dimension by two.

By leveraging the simplifying assumption of a constant low-thrust acceleration vector, additional insights are available to guide low-thrust trajectory design. Although H_{nat} does not represent a dynamically significant quantity in the CR3BP-LT (rather, it is merely a component of the low-thrust Hamiltonian, expressed in Equation (11)), it remains a useful reference to the natural CR3BP. Low-thrust arcs are frequently a means to transition between natural structures with fixed H_{nat} values, thus, the evolution of H_{nat} in the CR3BP-LT is of interest. While H_{nat} is not constant in general when low-thrust is active, H_{nat} evolves independently of the spacecraft path when \vec{a}_{lt} is fixed in the rotating frame. This property is available from the time-derivative of H_{nat} , expressed in Equation (18). As the \vec{a}_{lt} vector is constant, this expression is integrable, yielding the equation

$$H_{nat}(\tau_f) - H_{nat}(\tau_0) = \int_{\tau_0}^{\tau_f} \vec{v} \cdot \vec{a}_{lt} \, d\tau = (\vec{r}(\tau_f) - \vec{r}(\tau_0)) \cdot \vec{a}_{lt}. \quad (22)$$

Accordingly, the natural Hamiltonian value along any low-thrust arc is available given the initial H_{nat} value, the initial and final position, and the fixed low-thrust acceleration vector. This relationship supplies useful insights that link the geometry of low-thrust arcs to the evolution of H_{nat} , facilitating intuitive design strategies.

Finally, to further reduce the system complexity, only planar motion is explored. Thus, $z(\tau) = \dot{z}(\tau) = 0$ for all τ , and the low-thrust pointing vector, \hat{u} , is described by the planar vector

$$\hat{u} = \left\{ \cos \alpha \quad \sin \alpha \quad 0 \right\}^T. \quad (23)$$

These simplifications facilitate the analysis of dynamical structures in the CR3BP-LT while also supplying insights that are useful for spatial (3D) path planning.

ENERGY PLANES

In the planar CR3BP-LT, every low-thrust arc with \vec{a}_{lt} fixed in the rotating frame lies entirely within a plane oriented in x - y - H_{nat} space by the low-thrust orientation angle, α , and the magnitude, a_{lt} . This *energy plane* includes the initial position and energy along the low-thrust arc, defined by an initial *control point*, $\vec{\rho}_0 = \{x_0 \ y_0 \ H_{nat,0}\}^T$. A low-thrust trajectory may be represented by the control point variation,

$$\Delta \vec{\rho}(\tau) = \vec{\rho}(\tau) - \vec{\rho}_0 = \Delta x \hat{x} + \Delta y \hat{y} + \Delta H \hat{H} \quad (24)$$

where $\vec{\rho}(\tau) = \{x(\tau) \ y(\tau) \ H_{nat}(\tau)\}^T$ is a control point that reflects the spacecraft position and energy at nondimensional time τ . Accordingly, $\Delta \vec{\rho}(\tau)$ locates the spacecraft relative to the origin

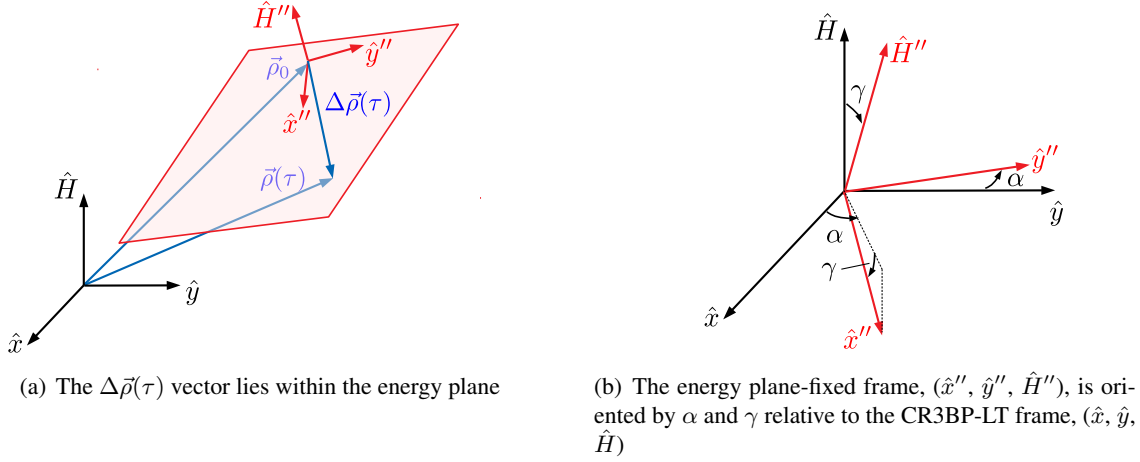


Figure 2. The energy plane is located and oriented relative to the rotating x - y frame with a third dimension representing H_{nat} .

of the energy plane, as depicted in Figure 2(a). The plane is oriented via two rotations: a rotation of α about $\hat{H} = \hat{H}'$ to the intermediate frame, $(\hat{x}', \hat{y}', \hat{H}')$, followed by a rotation of γ about $\hat{y}' = \hat{y}''$ to a frame fixed in the energy plane, $(\hat{x}'', \hat{y}'', \hat{H}'')$, as seen in Figure 2(b). The first angle, α , orients the low-thrust acceleration vector, as noted in Equation (23). The second rotation angle, γ , is related to the low-thrust acceleration magnitude via the relationship

$$\tan \gamma = -a_{lt}. \quad (25)$$

As a short proof that such a plane exists with this orientation, rewrite the general control point variation in Equation (24) in the energy plane-fixed frame,

$$\Delta\vec{\rho} = [\Delta x C_\alpha C_\gamma + \Delta y S_\alpha C_\gamma - \Delta H S_\gamma] \hat{x}'' + [\Delta y C_\alpha - \Delta x S_\alpha] \hat{y}'' + [\Delta x C_\alpha S_\gamma + \Delta y S_\alpha S_\gamma + \Delta H C_\gamma] \hat{H}'' , \quad (26)$$

where $C_\alpha = \cos \alpha$, $S_\alpha = \sin \alpha$, $C_\gamma = \cos \gamma$, and $S_\gamma = \sin \gamma$. A trajectory confined to the plane possesses a zero-valued \hat{H}'' component, thus, rearrange the terms in the \hat{H}'' coordinate and equate it to zero,

$$\Delta H + \tan \gamma (\Delta x C_\alpha + \Delta y S_\alpha) = 0. \quad (27)$$

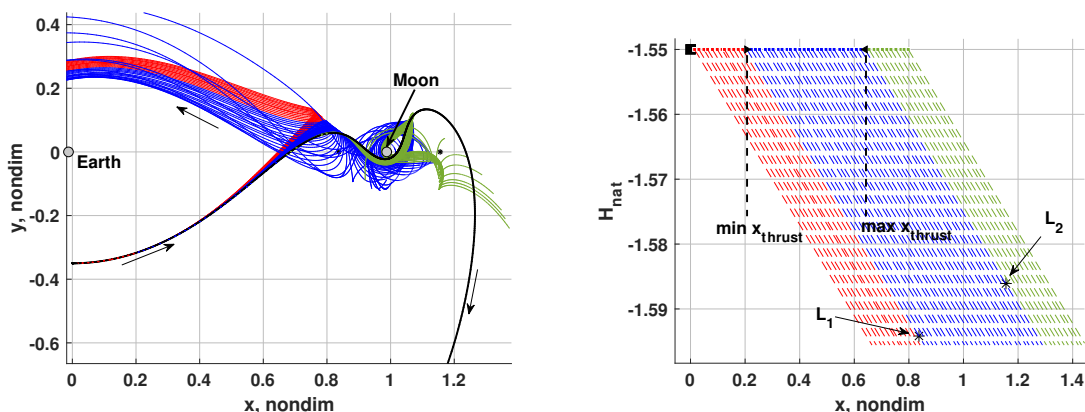
When Equation (25) is substituted for the $\tan \gamma$ term, Equation (27) is identical to the energy path-independence relationship in Equation (22). Subsequently, Equation (27) is truly equal to zero; the out-of-plane component of $\Delta\vec{\rho}(\tau)$ is identically zero for all τ and the low-thrust arc is confined to the energy plane while \vec{a}_{lt} remains fixed in the CR3BP-LT rotating frame. This plane is leveraged to link a particular energy change to the geometry of a low-thrust transfer arc. If the geometry of such a transfer is relatively unperturbed by the low-thrust acceleration vector, α and a_{lt} may be selected to orient the energy plane to deliver a desired energy change based on the existing geometry. Additionally, these results validate previous findings that the energy along low-thrust arcs varies as a function of the angle between the low-thrust acceleration vector and the spacecraft velocity vector, i.e., the angle between \hat{u} and \vec{v} .¹² When \vec{v} is aligned with \hat{u} , the spacecraft moves “uphill” on the energy plane, increasing the H_{nat} value. Similarly, a spacecraft with $\hat{u} \perp \vec{v}$ progresses across the energy plane at a constant value of H_{nat} . While these properties of the H_{nat} value are

straightforwardly derived from the time derivative in Equation (18), the energy plane supplies a more intuitive representation of the energy variations. Similar to a hiker faced with a steep slope, a low-thrust spacecraft may leverage sequential energy planes as a set of “switchbacks” to rapidly increase energy. In fact, the well-known energy-optimal low-thrust spiral that employs a control law with $\hat{u} = \hat{v}$ is simply a strategy to continuously reorient the energy plane such that the spacecraft is always moving along the steepest energy gradient.

GATEWAY MANIPULATION USING ENERGY PLANES

Bounds on the spacecraft motion in the natural CR3BP, termed *forbidden regions*, are linked to the instantaneous value of H_{nat} along a trajectory, thus, information about the evolution of H_{nat} provided by an energy plane is useful to plan for desirable configurations of the forbidden regions.¹⁵ The H_{nat} values associated with the natural equilibrium solutions are significant as they represent critical H_{nat} values at which the forbidden regions shrink (or grow) to permit (or restrict) access to specific locations in the rotating frame. For example, for H_{nat} values slightly higher than the $H_{nat}(L_1)$ value, the forbidden regions include a narrow neck near the L_1 point, i.e., a “gateway,” through which trajectories may pass to transit between the P_1 and P_2 regions. Similar gateways form as H_{nat} increases past the L_2 and L_3 energy levels, and the H_{nat} value corresponding to the $L_{4/5}$ equilibrium points is the highest energy for which planar motion is restricted by the forbidden regions in the CR3BP. Accordingly, to enable transit between regions of the rotating frame, the H_{nat} value along an arc is specified to achieve a desirable forbidden region configuration. Furthermore, as the energy along a low-thrust arc is described by an energy plane, the coupled geometry-energy challenge in navigating a gateway is mitigated by leveraging the energy plane.

To illustrate the manipulation of the forbidden regions via insights from an energy plane, consider a ballistic path that passes from the system interior (i.e., near P_1) through the L_1 and L_2 gateways to the exterior region, as plotted in black in Figure 3(a). Assume that the path must be modified



(a) Arcs plotted in configuration space

(b) Initial states are represented by squares and the energy plane for each arc is plotted as a dashed line

Figure 3. The transit behaviors of low-thrust arcs (colored) in the Earth-Moon CR3BP-LT for $a_{lt} = 7e-2$ and $\alpha = 180^\circ$ originating from different locations on a ballistic arc (black) are predicted by a simple trigonometric property of the energy plane geometry

to prohibit one or both gateway transits. To avoid escape to the system exterior, it is sufficient to

reduce the H_{nat} value along the low-thrust arc such that, at the location of the L_2 gateway transit, the spacecraft H_{nat} value is lower than $H_{nat}(L_2)$. Further energy reductions may restrict the spacecraft to the vicinity of P_2 , or prohibit transit into the P_2 region entirely by closing the L_1 gateway. Given a low-thrust acceleration magnitude and orientation, limits on the thrust timing are available from the associated energy planes. The last location along the ballistic arc where low-thrust may be leveraged to sufficiently lower the H_{nat} value and prohibit transit through the L_2 gateway is computed via a trigonometric relationship. Let $\alpha = 180^\circ$ to orient the energy plane such that H_{nat} decreases as the spacecraft moves toward larger x values. Accordingly, a maximum x value is computed as follows,

$$\max x_{thrust} = x_{L_2} - \frac{1}{a_{lt}} [H_{nat,0} - H_{nat}(L_2)] , \quad (28)$$

where $H_{nat,0}$ is the energy of the ballistic arc and x_{L_2} is the position of L_2 on the x -axis. If the low-thrust force is switched on after the spacecraft has progressed to a location such that $x > \max x_{thrust}$, the energy on the resulting low-thrust arc will not decrease sufficiently to close the L_2 gateway. Thus, when the spacecraft reaches x_{L_2} , the spacecraft may escape the system through the L_2 gateway. A similar minimum x -coordinate is available that marks the last location along the path where the low-thrust force may be activated to close the L_1 gateway at x_{L_1} ,

$$\min x_{thrust} = x_{L_1} - \frac{1}{a_{lt}} [H_{nat,0} - H_{nat}(L_1)] . \quad (29)$$

These bounds, identified as black triangles in Figure 3(b), are employed to categorize a set of low-thrust arcs, all originating from the ballistic path at different x locations. Red arcs, plotted in the xy -plane in Figure 3(a), initiate thrusting at $x < \min x_{thrust}$. Similarly, green arcs depart the ballistic arc at locations such that $x > \max x_{thrust}$. Arcs that commence thrusting between these two bounds are plotted in blue. The energy plane analysis predicts that red arcs will fail to transit the L_1 gateway as the energy along these trajectories decreases below the L_1 gateway energy, i.e., the L_1 gateway is closed when the low-thrust arc arrives at the gateway. This prediction is supported by the results in Figure 3(a); all of the red arcs remain in the interior region. The energy planes associated with these arcs, plotted as dashed lines in Figure 3(b), visually demonstrate that the energy along each red arc decreases to $H_{nat}(L_1)$ before or at x_{L_1} . In contrast, as the blue arcs activate thrust forces sufficiently late to avoid closing the L_1 gateway before passing through, they may transit into the P_2 region but will not pass through the L_2 gateway. This result is also supported by the plot, as many blue arcs enter the P_2 region and none transit the L_2 gateway. However, a subset of these trajectories do not pass through the L_1 gateway; while the energy on these paths at the L_1 gateway is sufficiently high to permit transit, transit is not guaranteed. Finally, the green arcs add thrust at locations where $x > \max x_{thrust}$, thus, the H_{nat} values on these arcs are sufficiently high to allow transit through the L_2 gateway; again this is a sufficient condition and does not guarantee transit, as evident from the configuration space representation in Figure 3(a). This analysis demonstrates that the energy plane is a useful tool to predict the transit or capture behavior of a low-thrust arc. The geometry of the ballistic transit arc employed in this example (seen in black in Figure 3(a)) is only slightly modified by a low-thrust force during the approach to the P_2 vicinity, thus, the energy along the low-thrust arcs is straightforwardly controlled as the path moves predictably along the prescribed energy plane. However, as the arcs traverse the dynamic regions near L_1 , P_2 , and L_2 , the trajectory geometry is significantly affected by the addition of low-thrust and, thus, is more difficult to predict. Regardless of these sensitivities, the energy along each low-thrust arc is confined to the energy plane and transit (or capture) is well-predicted by the sufficient conditions derived from the

energy history. This strategy is also applicable to scenarios other than gateway transit behavior; any problem that requires a specific energy value at a specific location (i.e., targeting a control point) is facilitated by the CR3BP-LT energy planes.

PLANAR LOW-THRUST EQUILIBRIUM SOLUTIONS

While insights from the energy plane are useful to modify ballistic paths, dynamical structures from the CR3BP-LT supply additional geometries that may be leveraged to facilitate low-thrust trajectory design. One such set of structures are the equilibrium solutions associated with the planar (2D) dynamics in the CR3BP-LT; these solutions supply an initial characterization of the local and global dynamics when low-thrust is included in the model. Linearizations of the nonlinear dynamics relative to the equilibria describe local stable, unstable, and center manifolds. Global invariant manifolds are constructed by transitioning the linear results to the nonlinear model.¹⁵ Manipulations of the low-thrust acceleration vector directly influence the number and location of equilibrium solutions in the CR3BP-LT, which subsequently affects the existence and characteristics of various nearby dynamical structures. Accordingly, the equilibrium solutions in the CR3BP-LT are relevant to low-thrust mission applications, particularly as the equilibria locations evolve relative to the familiar CR3BP equilibrium points.

To initiate a fundamental understanding of the flow in the CR3BP-LT, consider the simplified planar dynamics with a fixed \vec{a}_{lt} vector, consistent with the previously presented simplifications. The equilibrium solutions solve Equations (13) and (14) when all time derivatives (\dot{x} , \ddot{x} , \dot{y} , \ddot{y}) are zero. In the natural CR3BP ($a_{lt} = 0$), five such equilibria exist, i.e., the *Lagrange points* or *libration points*.¹⁵ As the addition of the perturbing low-thrust acceleration introduces two new variables, the thrust orientation angle, α , and magnitude, a_{lt} , the locations of the equilibrium solutions are no longer fixed.^{12,13,14} Given a value of a_{lt} , the locations of the equilibrium solutions vary with α , as plotted in Figure 4. The location of each equilibrium solution identifies a point in the xy -

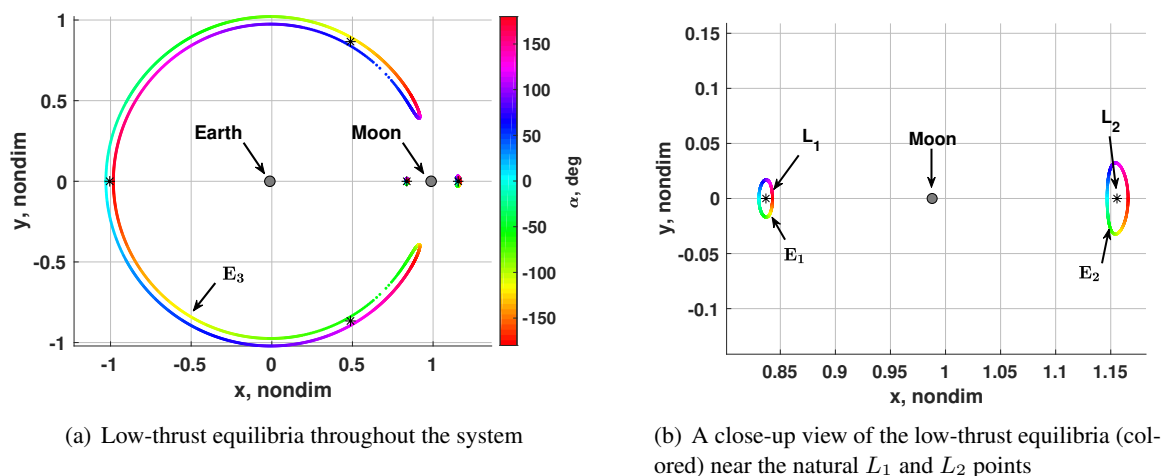


Figure 4. Low-thrust equilibrium solutions (colored by α) in the Earth-Moon CR3BP-LT for $a_{lt} = 7e-2$ and $\alpha \in [-\pi, \pi]$; the natural equilibrium solutions are included as black asterisks

plane where the low-thrust acceleration vector offsets the natural acceleration vector to yield a net-zero acceleration in the rotating frame. Accordingly, the closed, colored contours of equilibria

depicted in Figure 4 are termed *zero acceleration contours* (ZACs).¹² Each ZAC represents a set of equilibria at a fixed a_{lt} value for the full range of α values with at least one equilibrium solution on each ZAC for every value of α . To identify these structures independently of the natural equilibria point solutions, let the ZACs near L_1 and L_2 be notated \mathbb{E}_1 and \mathbb{E}_2 , and let the C-shaped ZAC that includes points near L_3 be labeled \mathbb{E}_3 . These designations are specific to the a_{lt} value that yields the ZACs. For instance, when a_{lt} is small, the ZACs remain near the natural solutions, yielding five ZACs: $\mathbb{E}_1, \mathbb{E}_2, \dots, \mathbb{E}_5$. However, as a_{lt} increases, ZACs merge. In this investigation, $a_{lt} = 7e-2$ is employed for consistency; at this low-thrust magnitude, the $\mathbb{E}_3, \mathbb{E}_4$ and \mathbb{E}_5 structures are merged into the \mathbb{E}_3 ZAC. Distinct sets of equilibria at specific α values are denoted via function notation, i.e., $\mathbb{E}_3(-60^\circ)$ specifies the low-thrust equilibria on \mathbb{E}_3 at $\alpha = -60^\circ$. To identify specific equilibrium points on a ZAC, or within a set of equilibria at a specific angle on a ZAC, the notation $E_i^j(\alpha)$ is employed, where i references the ZAC, \mathbb{E}_i , and j designates the individual equilibria in order of ascending H_{lt} value. For example, $\mathbb{E}_3(-60^\circ)$ includes three equilibria, thus, $E_3^1(-60^\circ)$ corresponds to the equilibria with the lowest H_{lt} value, $E_3^2(-60^\circ)$ possesses an intermediate H_{lt} value, and $E_3^3(-60^\circ)$ is characterized by the highest H_{lt} value. In the absence of a superscript, e.g., $E_1(-60^\circ)$, only one equilibrium solution exists on the specified ZAC at the given angle.

As the locations of the low-thrust equilibrium solutions change with variations in a_{lt} and α , the stability of each point also varies. The stability corresponding to a low-thrust equilibrium solution is determined by inspecting the eigenvalues of the Hessian matrix, $\partial^2 \vec{q} / \partial \vec{q}$, evaluated at the equilibrium point location where $\vec{q} = \{x, y, \dot{x}, \dot{y}\}^T$ is the state vector and \vec{q} reflects the time derivatives of the states consistent with Equations (13) and (14).^{12,14} Real eigenvalues (in the complex plane) represent stable (negative) and unstable (positive) motion, while eigenvalues on the imaginary axis represent oscillatory motion. Combinations of the two types are also possible and are characterized by spiral-shaped flow patterns. Due to the Hamiltonian nature of the CR3BP-LT with \vec{a}_{lt} fixed in the rotating frame, eigenvalues occur in pairs, either as real pairs symmetric across the imaginary axis (i.e., $\pm\lambda$) or as complex conjugate pairs. The former pair, characterized by stable and unstable motion, is termed a *saddle*, while a pair of imaginary eigenvalues is denoted a *center* mode; the combined saddle-center (e.g., spiral) motion is termed a *mixed* mode.

The linear modes associated with an equilibrium solution identify the local dynamics and can predict nonlinear flow patterns. For example, oscillatory motion (periodic or quasi-periodic) is available near an equilibrium solution with a center mode, or a center subspace. Similarly, trajectories that asymptotically approach an equilibrium point in forward and reverse time are guided by the stable and unstable manifolds of the saddle mode. The four-dimensional phase space near each planar equilibrium point is described by four eigenvalues (two pairs), or two modes. In practice, these modes occur in four different combinations: (i) saddle \times center; (ii) center \times center; (iii) mixed \times mixed; and (iv) saddle \times saddle. The Earth-Moon CR3BP-LT equilibria for $a_{lt} = 7e-2$ are characterized by the first three combinations at various locations in the xy -plane, as apparent in Figure 5. The dynamics near equilibria on \mathbb{E}_1 and \mathbb{E}_2 are consistent with the saddle \times center motion associated with L_1 and L_2 , as observed in Figure 5(b). In contrast, \mathbb{E}_3 includes saddle \times center motion on the “inner ring,” center \times center motion on the “outer ring,” and some mixed \times mixed motion near the tips of the C-shaped contour. Due to the proximity of different linear modes, the low-thrust dynamics in some locations are very sensitive to the value of α employed to orient the low-thrust vector. For instance, both center \times center and saddle \times center equilibrium solutions are available near the L_4 and L_5 points at the same a_{lt} value and opposite (by 180°) α values. As a result, the global flow in a single area (e.g., near $L_{4/5}$) is controllable via manipulations of the

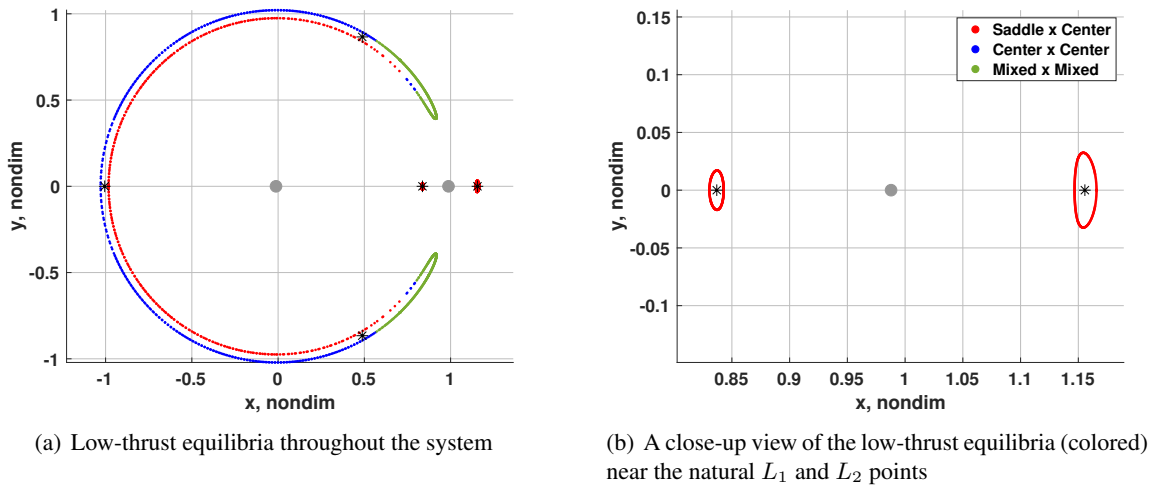


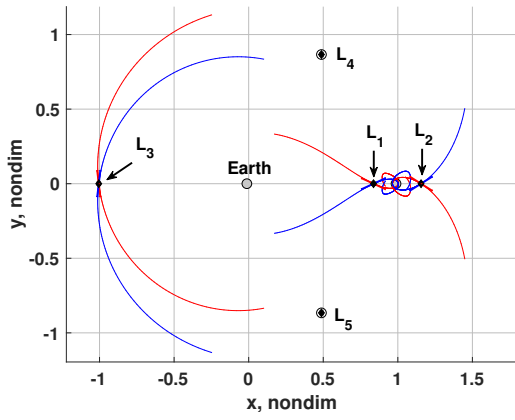
Figure 5. Low-thrust equilibrium solutions (colored by stability) in the Earth-Moon CR3BP-LT for $a_{lt} = 7e-2$ and $\alpha \in [-\pi, \pi]$; the natural equilibrium solutions are included as black asterisks

low-thrust acceleration vector and suitable parameters may be identified to yield flow structures for inclusion in low-thrust trajectories.

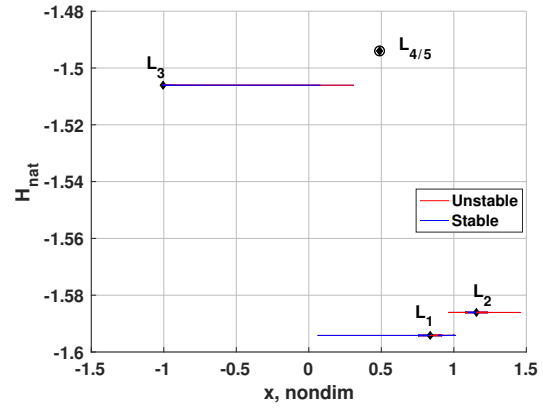
STABLE AND UNSTABLE INVARIANT MANIFOLDS

The linear dynamics in the vicinity of the low-thrust equilibrium points are straightforwardly transitioned to the full nonlinear model to supply insight into global flow patterns in the CR3BP-LT. Whereas the eigenvalues of the Hessian matrix describe the type of motion (e.g., stable, unstable, oscillatory), the eigenvector associated with each eigenvalue defines the direction of the flow in four-dimensional space. That is, the eigenvector associated with the positive, real eigenvalue lies tangent to the unstable manifold near the equilibrium solution. Similarly, the eigenvector associated with the negative, real eigenvalue is tangent to the stable manifold near the equilibrium point. Thus, by perturbing the equilibrium solution along the stable or unstable eigenvector and propagating the resulting trajectory in the nonlinear model, a representation of the global stable or unstable invariant manifold associated with the equilibrium point is constructed, as depicted for the natural L_1 , L_2 , and L_3 saddle modes in Figure 6. While these manifolds originate tangent to the eigenvectors (represented by small, colored arrows) near the equilibria, the nonlinear flow diverges from the linear approximation as the distance from the equilibrium solution increases. The natural triangular points, characterized by center \times center modes, do not possess stable or unstable manifolds to guide flow into and out of the L_4 or L_5 regions. Additionally, note that the H_{nat} value along each manifold remains constant, as evident in Figure 6(b), as H_{nat} is a constant integral of the motion in the natural CR3BP.

Similar manifolds are constructed in the Earth-Moon CR3BP-LT, but these low-thrust structures include key differences. For example, the Earth-Moon low-thrust equilibria for $a_{lt} = 7e-2$ and $\alpha = 180^\circ$, plotted as black diamonds in Figure 7(a), are similar in location and stability to the natural equilibria, though the $\mathbb{E}_3(180^\circ)$ solutions not located on the x -axis (i.e., $E_3^2(180^\circ)$ and $E_3^3(180^\circ)$) lie noticeably closer to the Moon than the natural triangular points. Furthermore, the geometries of the stable and unstable manifolds corresponding to the $E_1(180^\circ)$ and $E_2(180^\circ)$ points

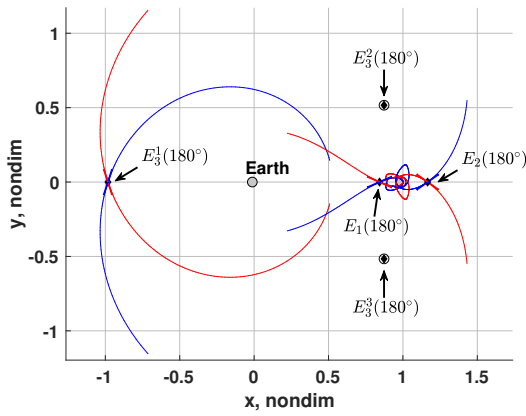


(a) Global manifolds in the xy -plane

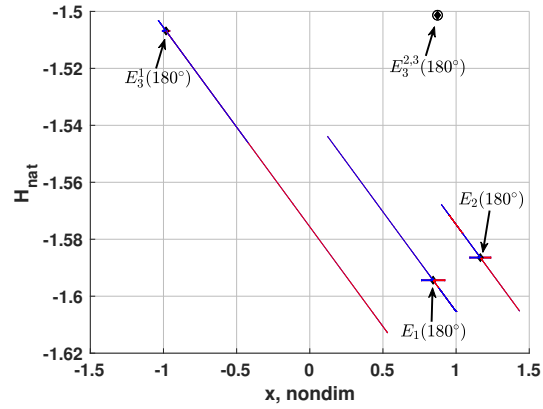


(b) The energy along each manifold is consistent with the energy of the originating equilibrium solution

Figure 6. Manifolds of the natural Earth-Moon CR3BP equilibria; L_1 , L_2 , and L_3 possess saddle modes with stable and unstable manifolds while L_4 and L_5 are characterized by center \times center modes, represented by circles about these equilibria



(a) Global manifolds in the xy -plane; note the new locations of the equilibria off of the x -axis with the addition of low-thrust



(b) The energy along each manifold varies with distance from the energy of the originating equilibrium solution

Figure 7. Manifolds of the Earth-Moon CR3BP-LT equilibria for $a_{lt} = 7e-2$ and $\alpha = 180^\circ$ maintain a similar geometry and qualitative stability characteristics as the natural equilibria manifolds, but vary in energy

remain very similar to the natural manifolds plotted in Figure 6(a). In addition to the shifted triangular point locations, a key difference between the low-thrust equilibria manifolds and the natural equilibria manifolds is the energy profile for each manifold, plotted in Figures 7(b) and 6(b), respectively. While H_{nat} is constant along the ballistic CR3BP arcs, H_{nat} varies with distance from the originating state along the low-thrust structures. Accordingly, the low-thrust equilibrium point manifolds may be employed to transit throughout the xy -plane while simultaneously delivering an energy change prescribed by the associated energy plane.

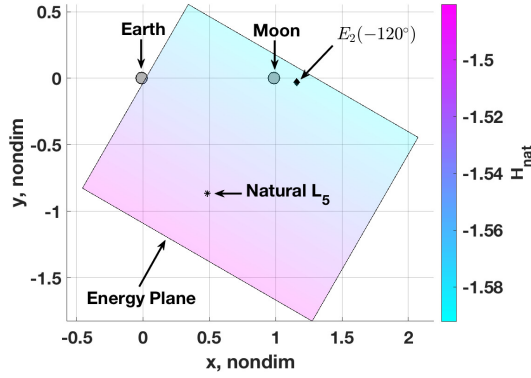
TRANSIT DESIGN LEVERAGING MANIFOLD ARCS

To illustrate the use of manifolds associated with the equilibrium points and the low-thrust energy plane, consider the design of a transfer from the lunar vicinity to a stable orbit near the natural Earth-Moon L_5 point. A design may be constructed from the manifolds associated with the L_1 and L_2 equilibria that depart the lunar vicinity and move throughout the xy -plane. However, these manifolds, plotted in Figure 6(a), do not approach the L_5 region, even when propagated for longer time intervals than depicted in the plot. Furthermore, these natural manifolds maintain a fixed H_{nat} value consistent with the originating equilibrium point and, thus, do not approach the much higher $H_{nat}(L_5)$ value. An additional complication arises from the fact that L_5 is characterized by center \times center motion and, thus, possesses no manifolds to further attract the flow. Farrés mitigates this problem when designing similar transfers in the Sun-Earth system that employ an additional force using a solar sail by using a “brute force search” to identify sail orientations and states near the triangular point that, when propagated in reverse time, may be linked to the $E_1(0)$ or $E_2(0)$ unstable manifolds in both position and energy to construct an end-to-end transfer design.¹³ By leveraging insights from energy planes and employing equilibrium solutions in the CR3BP-LT located near L_5 with nontrivial saddle modes, a transfer is straightforwardly designed without a grid search.

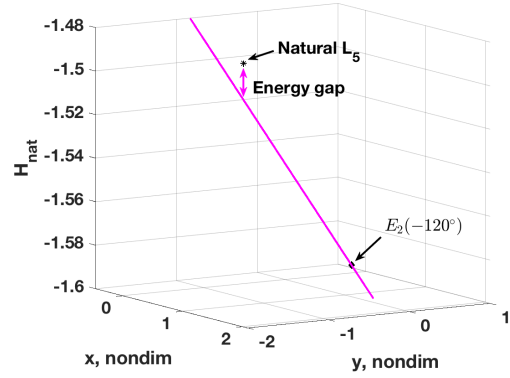
A transfer design that incorporates both the energetic and geometric differences between the L_5 and lunar regions is facilitated by leveraging manifolds of the low-thrust equilibria. Whereas the natural CR3BP equilibria manifolds maintain fixed H_{nat} values, H_{nat} varies along the low-thrust manifolds associated with the CR3BP-LT equilibria, as described by the energy plane corresponding to the α and a_{lt} values of the originating equilibrium point. Accordingly, the H_{nat} value along each manifold increases in the direction described by α . The \mathbb{E}_1 and \mathbb{E}_2 low-thrust equilibria remain within a small, bounded area (in position and H_{nat}) regardless of α , but the orientation of the energy plane associated with each equilibrium point varies linearly with α . Additionally, recall that the \mathbb{E}_1 and \mathbb{E}_2 structures for $a_{lt} = 7e-2$, depicted in Figure 5(b), are entirely characterized by saddle \times center modes, thus, unstable manifolds departing the lunar region are available for all values of α . A survey of these manifolds over the full range of α values indicates that, while small geometric differences are apparent as α varies, the general flow pattern (as visualized in Figure 7(a)) remains consistent. Thus, the energy on these manifolds may be designed relatively independently of the manifold geometry by selecting an α value to supply an appropriate energy plane, i.e., an energy plane sloped in a desirable direction.

To develop an initial guess for a transfer between the Moon and L_5 , the manifolds of an Earth-Moon CR3BP-LT \mathbb{E}_2 solution are explored (alternatively, manifolds corresponding to an \mathbb{E}_1 point may be leveraged). To maximize the H_{nat} value available at L_5 on a low-thrust arc originating from one of these equilibria, the energy plane is aligned with the Moon- L_5 line, e.g., $\alpha = -120^\circ$, as plotted in Figure 8. However, even with the plane oriented to maximize the energy at the L_5 location, the slope of the energy plane is too shallow to reach $H_{nat}(L_5)$ at the L_5 position, visualized as an “energy gap” between the energy plane and the L_5 point in x - y - H_{nat} space plotted in Figure 8(b). Accordingly, a single manifold originating from an \mathbb{E}_2 point cannot reach the natural L_5 point with the desired energy. Additional energy manipulations are required to construct a set of multiple “energy switchbacks” that reach both the L_5 position and energy level.

To facilitate an energy increase from $H_{nat}(L_2)$ to $H_{nat}(L_5)$, low-thrust flow originating near the natural L_5 point is linked to low-thrust flow near the Moon. In contrast to the natural CR3BP, the CR3BP-LT possesses equilibrium points near L_5 on the \mathbb{E}_3 structure with saddle \times center motion. In the Earth-Moon CR3BP-LT with $a_{lt} = 7e-2$, these equilibria, plotted as red points in Figure 5(a),



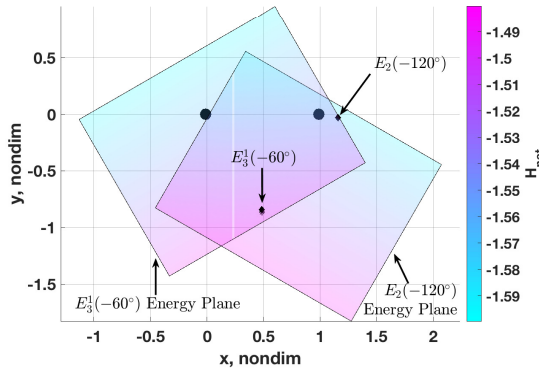
(a) Planar projection of the energy plane



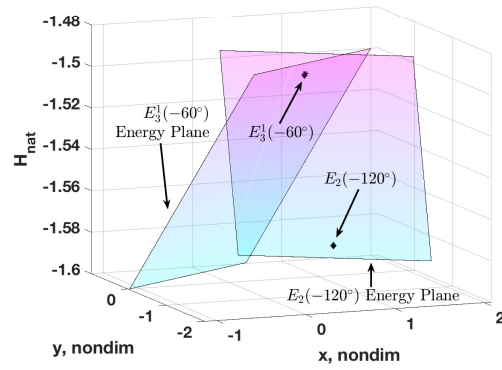
(b) Edge-on view of the energy plane; the natural L_5 point possesses an H_{nat} value higher than those attainable on the energy plane at the location of the L_5 point

Figure 8. The energy plane associated with the Earth-Moon CR3BP-LT $E_2(-120^\circ)$ point for $a_{lt} = 7e-2$ is too shallow to reach $H_{nat}(L_5)$ at the L_5 location

are located near L_5 when $\alpha \approx -60^\circ$. While the locations and energies of the equilibria on \mathbb{E}_1 and \mathbb{E}_2 vary only a small amount with α , the \mathbb{E}_3 equilibrium points shift over large distances throughout the xy -plane as α varies. Accordingly, only the $E_3^1(-60^\circ)$ solution near L_5 supplies manifolds that evolve sufficiently to attract flow. The energy profiles of these manifolds are defined by the energy plane oriented by $\alpha = -60^\circ$, i.e., the H_{nat} value along each manifold increases along the $P_1 \rightarrow L_5$ line, as depicted in Figure 9. A transfer from $E_2(-120^\circ)$ to $E_3^1(-60^\circ)$ may leverage flow along



(a) Planar projection



(b) 3D view in x - y - H_{nat} space

Figure 9. The energy planes corresponding to the low-thrust equilibrium points $E_3^1(-60^\circ)$ near L_5 and $E_2(-120^\circ)$ contain all trajectories originating from the two equilibria; control adjustments at the intersection of the two planes facilitates transfers between the two points

both energy planes. Such a transfer originates at the $E_2(-120^\circ)$ point and subsequently flows along the corresponding energy plane. Then, at an intersection between the $E_2(-120^\circ)$ energy plane and the $E_3^1(-60^\circ)$ energy plane, the low-thrust parameters may be switched to match those associated with the $E_3^1(-60^\circ)$ point, i.e., α is switched from -120° to -60° . The resulting propagation then

flows along the $E_3^1(-60^\circ)$ energy plane, which includes the $E_3^1(-60^\circ)$ equilibrium solution very near the location and energy of the natural L_5 point, facilitating the required energy change.

The intersection of two energy planes defines a line in x - y - H_{nat} space that is leveraged as a hyperplane for the comparison of states on the two energy planes. Define a reference control point anywhere on the line, $\vec{\rho}_{ref}$, and let l represent the distance from $\vec{\rho}_{ref}$ along the xy -projection of the line with $l > 0$ corresponding to increasing values of H_{nat} . That is, l represents the physical distance between $\vec{\rho}_{ref}$ and another point on the line. The set of control points on the intersection line, $\mathcal{H}_{1,2}$, are given by

$$\mathcal{H}_{1,2} : \vec{\rho} = \vec{\rho}_{ref} + l\vec{H}_{int}, \quad (30)$$

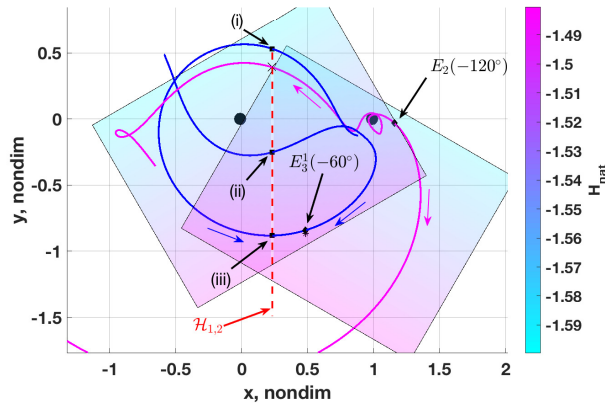
where \vec{H}_{int} is derived from the cross product of the two energy plane normal vectors, \hat{H}_1'' and \hat{H}_2'' ,

$$\vec{H}_{int} = \left\{ \cos([\alpha_1 + \alpha_2]/2) \quad \sin([\alpha_1 + \alpha_2]/2) \quad a_{lt} \cos([\alpha_2 - \alpha_1]/2) \right\}^T, \quad (31)$$

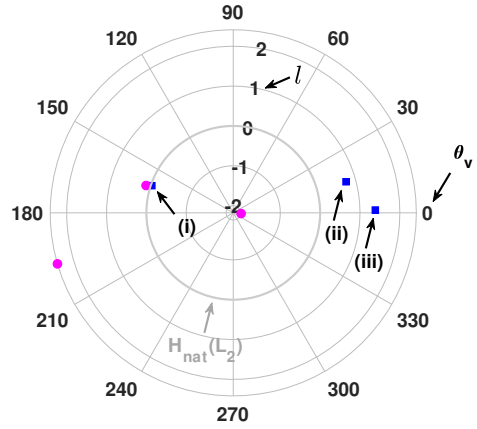
and both energy planes correspond to the same a_{lt} value (i.e., the same γ angle) but different α values. The \vec{H}_{int} vector supplies the normalized slope of the planar projection of the intersection line in the first two components as well as the scaled energy slope in the third component to deliver H_{nat} given $\vec{\rho}_{ref}$ and l . To identify trajectories with similar positions and velocities on $\mathcal{H}_{1,2}$, the planar projection of the intersection line is leveraged as a stopping condition, i.e., a hyperplane $\Sigma_{\mathcal{H}_{1,2}}$, for low-thrust manifolds propagated from the $E_2(-120^\circ)$ and $E_3^1(-60^\circ)$ points. Because $\mathcal{H}_{1,2}$ defines points that lie on both energy planes, proximity between two points (i.e., similar l values) on the projection, $\Sigma_{\mathcal{H}_{1,2}}$, indicates not only similar positions in the xy -plane, but also similar H_{nat} values. Furthermore, a switch from α_1 to α_2 at $\Sigma_{\mathcal{H}_{1,2}}$ ensures that the trajectory transitions from the first energy plane to the second and, thus, is capable of reaching $H_{nat}(L_5)$ at the L_5 location.

While the distance along $\Sigma_{\mathcal{H}_{1,2}}$ relative to $\vec{\rho}_{ref}$, represented by l , supplies position and energy information, an additional coordinate is required to represent the full spacecraft state. Given l , the spacecraft position and H_{nat} value are computed via Equation (30). Additionally, the velocity magnitude at this point is available by solving the H_{nat} expression in Equation (3) for v . Only the velocity direction is undefined, thus, a Poincaré map leveraging the coordinates l and $\theta_v = \arctan(\dot{y}/\dot{x})$ supplies the complete spacecraft state; intersections on this map guarantee full state continuity between trajectories. Such a map is leveraged to identify a transfer between the unstable manifolds of $E_2(-120^\circ)$, plotted in magenta in Figure 10(a), and the stable manifolds of $E_3^1(-60^\circ)$, plotted in blue. Each manifold crosses the the hyperplane (dashed red in Figure 10(a)), $\Sigma_{\mathcal{H}_{1,2}}$ (or, equivalently, $\mathcal{H}_{1,2}$ in x - y - H_{nat} space), at least once. The hyperplane crossing points are transformed to l and θ_v coordinates and plotted in polar form on the Poincaré map in Figure 10(b). Each $\Sigma_{\mathcal{H}_{1,2}}$ crossing on the $E_3^1(-60^\circ)$ stable manifolds is marked by a black square and labeled with a lowercase roman numeral to link the points between configuration space and the map. The $E_2(-120^\circ)$ unstable manifold crossings are marked by “x” symbols; these crossings are left unlabeled as several occur far from the primaries and are not depicted in Figure 10(a). In this example, $\vec{\rho}_{ref}$ is selected such that the reference H_{nat} value is identical to the natural L_2 energy. Accordingly, $l > 0$ corresponds to energies greater than $H_{nat}(L_2)$ and $l < 0$ indicates lower energy values; the boundary at $l = 0$ is plotted in gray in Figure 10(b) for reference.

By leveraging the information available from the Poincaré map, a transfer from the Moon to L_5 is constructed. Two points near $l = 0$ and $\theta_v = 160^\circ$, one from a stable manifold and another from



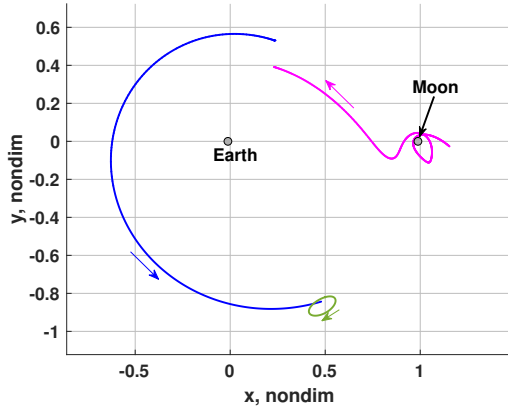
(a) xy -projection of the manifolds crossing the energy plane intersection line (dashed red) multiple times



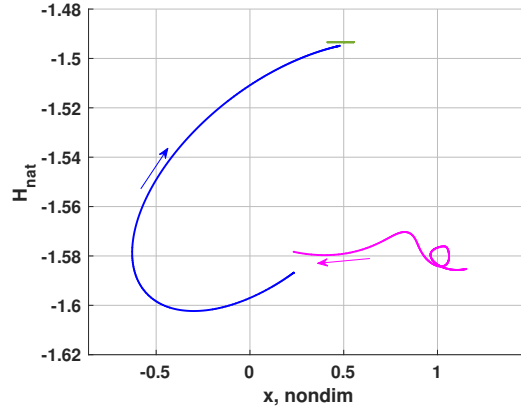
(b) Poincaré map of the manifolds at the energy plane intersection

Figure 10. The stable manifolds (blue) of the low-thrust L_5 point for $\alpha = -60^\circ$ and the unstable manifolds (magenta) of the low-thrust L_2 point for $\alpha = -120^\circ$ are propagated in the Earth-Moon CR3BP-LT for $a_{lt} = 7e-2$; crossings of the energy plane intersection line are marked and included in a Poincaré map to identify a transfer with minimal discontinuities

an unstable manifold, are selected due to their close proximity on the map. The corresponding manifolds, plotted in blue and magenta in Figure 11, are discontinuous in position, velocity, and natural Hamiltonian value. Thus, some corrections are required. To preserve the lunar flybys, the initial



(a) The arcs are discontinuous in position



(b) An additional energy discontinuity is apparent

Figure 11. The unstable $E_2(-120^\circ)$ manifold (magenta), stable $E_3^1(-60^\circ)$ manifold (blue), and natural L_5 short period orbit (green) are linked together as an initial design for a Moon to L_5 transfer

state on the $E_2(-120^\circ)$ unstable manifold is constrained in position and energy. Additionally, near the destination, a single revolution of a small, natural L_5 short period orbit is included to ensure the spacecraft remains near L_5 after arrival; this orbit is fully constrained to preserve its geometry and energy. Each manifold is subdivided into smaller segments, each of which maintains a fixed α value and a thrust magnitude of $a_{lt} = 7e-2$. A multiple shooting differential corrections algorithm is then applied to reduce the position and velocity discontinuities between the arcs, resulting in the

transfer plotted as a continuous solid arc in Figure 12. The initial design is first corrected in the

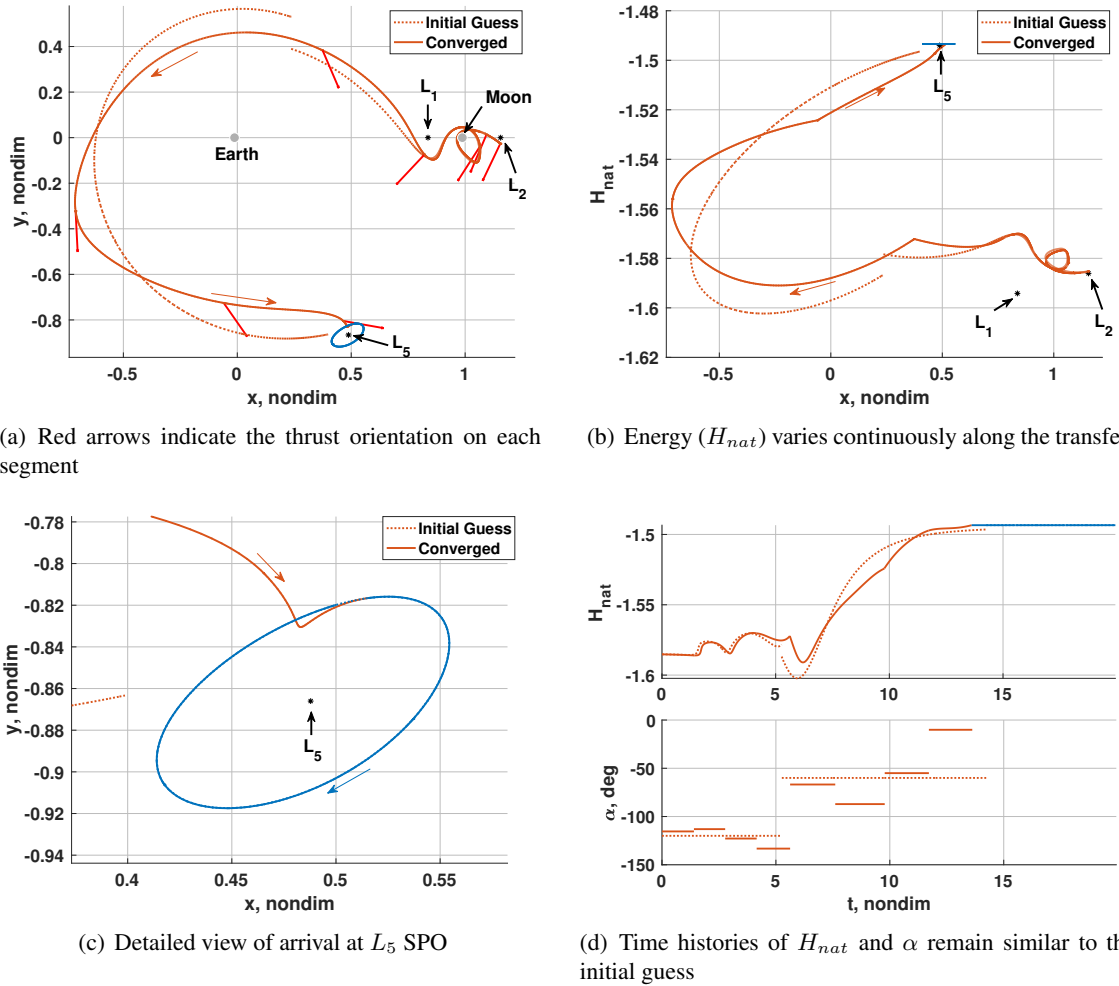


Figure 12. Following corrections, the transfer is continuous in position and velocity and energy; the majority of the transfer leverages low-thrust (orange segments) to reach the natural L_5 SPO (blue)

simplified CR3BP-LT with constant a_{lt} on all low-thrust arcs. Following convergence in the simplified model, the transfer is transitioned to the unsimplified CR3BP-LT with variable mass (i.e., variable $a_{lt} = f/m$) and an engine efficiency of $I_{sp} = 3000$ seconds. Although the initial design is constructed by leveraging insights from the simplified model with a constant a_{lt} value, convergence is rapid. The final spacecraft mass along the converged trajectory in Figure 12 is 0.9668, thus, the spacecraft requires propellant equivalent to approximately 3.32% of the spacecraft wet mass to complete the transfer. This mass fraction may be reduced further by applying optimization techniques, but represents a feasible scenario even without optimization (Deep Space 1, with low-thrust capabilities consistent with this example, was equipped with 82 kg of Xenon propellant for maneuvers, i.e., about 17% of the spacecraft wet mass*).

As the initial design, represented by dashed arcs, includes minimal discontinuities, the converged

*See the Deep Space 1 Asteroid Flyby press kit, https://www.jpl.nasa.gov/news/press_kits/ds1asteroid.pdf

solution consequently maintains the geometry of the initial guess in x - y - H_{nat} space. Additionally, the control history, plotted in Figure 12(d), remains similar to the preliminary solution with $\alpha \approx -120^\circ$ for the first 5.5 time units and reaches $\alpha \approx -60^\circ$ over the duration of the final thrust segments. These similarities are not surprising as the differential corrections algorithm employs an update that minimizes the variations from the initial design (i.e., a “minimum-norm” update). While the convergence properties of the algorithm depend on many variables, including the numerical implementation strategy, convergence is generally more rapid and more consistent with the initial design when the discontinuities are initially small; a poor (i.e., very discontinuous) input forces the differential corrections algorithm to make more significant changes to the design to meet the specified constraints. Thus, by leveraging insights from the CR3BP-LT, an initial design is straightforwardly constructed with minimal discontinuities in both configuration space and energy that may be rapidly corrected. In contrast to transfer construction procedures employing only arcs from the natural CR3BP, these low-thrust dynamical insights supply a preliminary control profile (i.e., α for the low-thrust segments) that subsequently delivers a suitable transfer geometry and a suitable energy profile.

CONCLUSION

By leveraging reasonable simplifying assumptions, the high-dimensional, non-conservative low-thrust multi-body model is reduced to a simpler, conservative system with properties that supply useful insights for the generation of preliminary low-thrust trajectory designs. One such property is the existence of an energy plane that describes the evolution of the natural Hamiltonian term along any low-thrust arc. The geometry of the plane mitigates the challenge of specifying an initial guess for the low-thrust acceleration vector magnitude and orientation, i.e., an initial guess for the control history. To demonstrate the usefulness of this plane, the transit and capture properties of various low-thrust arcs originating from a ballistic transit path are characterized by employing simple trigonometric insights from the energy plane. Additionally, a transfer between the Moon and L_5 Lagrange point is designed by leveraging multiple energy planes to deliver the required geometric and energetic trajectories.

ACKNOWLEDGEMENTS

The authors wish to thank the Purdue University School of Aeronautics and Astronautics for the facilities and support, including access to the Rune and Barbara Eliassen Visualization Laboratory. Additionally, many thanks to the Purdue Multi-Body Dynamics Research Group, the JPL Mission Design and Navigation branch, and Dan Grebow for interesting discussions and ideas. This research is supported by a National Aeronautics and Space Administration (NASA) Space Technology Research Fellowship, NASA Grant NNX16AM40H.

REFERENCES

- [1] G. Mingotti, F. Toppato, and F. Bernelli-Zazzera, “Combined Optimal Low-Thrust and Stable-Manifold Trajectories to the Earth-Moon Halo Orbits,” *AIP Conference Proceedings*, AIP, 2007.
- [2] J. Stuart, *A Hybrid Systems Strategy for Automated Spacecraft Tour Design and Optimization*. PhD Dissertation, Purdue University, West Lafayette, Indiana, May 2014.

- [3] G. Mingotti, F. Topputo, and F. Bernelli-Zazzera, “Optimal Low-Thrust Invariant Manifold Trajectories via Attainable Sets,” *Journal of Guidance, Control, and Dynamics*, Vol. 34, November 2011, pp. 1644–1656.
- [4] A. Das-Stuart, K. C. Howell, and D. C. Folta, “A Rapid Trajectory Design Strategy for Complex Environments Leveraging Attainable Regions and Low-Thrust Capabilities,” *68th International Astronautical Congress*, Adelaide, Australia, September 2017.
- [5] D. Grebow, M. Ozimek, and K. Howell, “Design of Optimal Low-Thrust Lunar Pole-Sitter Missions,” *The Journal of the Astronautical Sciences*, Vol. 58, January–March 2011, pp. 55–79.
- [6] R. Pritchett, E. Zimovan, and K. C. Howell, “Impulsive and Low-Thrust Transfer Design between Stable and Nearly Stable Periodic Orbits in the Restricted Problem,” *AIAA SciTech Forum*, Kissimmee, Florida, January 2018.
- [7] W. S. Koon, M. W. Lo., J. E. Marsden, and S. D. Ross, *Dynamical Systems, the Three-Body Problem and Space Mission Design*. New York: Springer, 2011.
- [8] M. W. Lo, B. G. Williams, W. E. Bollman, D. Han, Y. Hahn, J. L. Bell, E. A. Hirst, R. A. Corwin, P. E. Hong, K. C. Howell, B. T. Barden, and R. S. Wilson, “GENESIS Mission Design,” *The Journal of Astronautical Sciences*, Vol. 49, No. 1, 2001, pp. 169–184.
- [9] G. Gómez, J. Llibre, R. Martínez, and C. Simó, *Dynamics and Mission Design Near Libration Points, I: Fundamentals: The Case of Collinear Libration Points*. World Scientific Monograph Series, Singapore: Scientific Publishing, Ltd., 2001.
- [10] G. Gómez, W. Koon, M. Lo, J. Marsden, J. Masdemont, and S. Ross, “Connecting orbits and invariant manifolds in the spatial restricted three-body problem,” *Nonlinearity*, Vol. 17, No. 5, 2004, pp. 1571–1606.
- [11] F. Topputo, M. Vasile, and F. Bernelli-Zazzera, “Low energy interplanetary transfers exploiting invariant manifolds of the restricted three-body problem,” *Journal of Astronautical Sciences*, Vol. 53, No. 4, 2005, pp. 353–372.
- [12] A. D. Cox, K. C. Howell, and D. C. Folta, “Dynamical Structures in a Combined Low-Thrust Multi-Body Environment,” *AAS/AIAA Astrodynamics Specialist Conference*, Columbia River Gorge, Stevenson, Washington, August 2017.
- [13] A. Farrés, “Transfer orbits to L4 with a solar sail in the Earth-Sun system,” *Acta Astronautica*, Vol. 137, 2017, pp. 78–90.
- [14] A. D. Cox, K. C. Howell, and D. C. Folta, “Dynamical Structures in a Low-Thrust, Multi-Body Model with Applications to Trajectory Design,” (*currently under review*).
- [15] V. Szebehely, *Theory of Orbits: The Restricted Problem of Three Bodies*. New York: Academic Press, 1967.